Research Article

Fast synthesis of δ-MnO₂ for a high-performance supercapacitor electrode

Josué Marciano de Oliveira Cremonezzi[1,2] · Daniel Yaezu Tiba[1,2] · Sergio Humberto Domingues[1,2]

Abstract

We report a very simple and fast route for a high capacitive birnessite type manganese dioxide (δ-MnO₂) synthesis, fully suitable to be applied as electrode in redox-based electrochemical supercapacitors. The material was obtained from a very efficient chemical reduction of potassium permanganate by nascent hydrogen in low temperature acid media. δ-MnO₂ was extensively characterized by several techniques confirming the obtainment through the proposed route. The supercapacitive properties of the novel structure were evaluated showing a specific capacitance of 190 F g^{-1} at 0.25 A.g^{-1}. In addition, to the best of our knowledge, this is the first report regarding the chemical synthesis of δ-MnO₂ with no dependence of hazardous reducing agent, high temperature or high pressure commonly used to metal oxides production.

Keywords Delta manganese dioxide · Nascent hydrogen · Energy storage · Electrochemical capacitor

1 Introduction

Manganese dioxide (MnO₂) is the most studied metal oxide for redox-based electrochemical capacitors [1]. The main attractivities of MnO₂ are related to its low cost, environmental compatibility and tunable physical and chemical properties [2], among other advantages. The forehand MnO₂ energy storage application date from the late 1970s in lithium intercalation batteries [3–5]. Years later, in 1999, Goodenough and coworkers [6] observed the good capacitive response of amorphous MnO₂ as electrochemical capacitor electrode while looking for cheaper replacers to the expensive ruthenium oxides. Since then, several workers [7, 8] have dedicated attention to the understanding, synthesis and application of such extraordinary material.

MnO₂ structures are based in interlinked MnO₆ octahedrons ([MnO₆]), formed by 6 oxygen atoms on the vertices and a manganese atom on the center. Depending on the arrangement of the octahedrons, different layers and tunnels configurations are formed [9, 10]. Among several possible arrangements and stoichiometries, birnessite, also known as δ-MnO₂, is a layered structure with monoclinic arrangement of [MnO₆] sheets, with C2/m space group [11], containing mixtures of Mn(IV)/Mn(III) or Mn(IV)/Mn(II) and structural water in non-stoichiometric compositions [12, 13].

Electrochemical capacitors are considered a key solution for the energy storage systems required in the sustainable and renewable energy scenario that society needs to move into [1]. Two different mechanisms of capacitance are possible to occur in an electrode/electrolyte interface: the accumulation of ions in a electrochemical double layer (ECDL) or electrons transference via redox reactions, known as pseudocapacitance [14]. Due to its layered structure, δ-MnO₂ is claimed to be one of the few materials that shows both capacitive mechanisms concomitantly

[15, 16]. However, specific capacitance of birnessites, and other MnO_2 crystallographic phases as well, are highly dependent of several features [10]. The morphology [8, 17], the amount of defects [8], the Mn(IV)/Mn(III) relation [18], among other parameters are decisive in the material's capacity of storing tens or hundreds of farads per gram.

Thus, the search for phase selective MnO_2 synthesis methods is still a challenging and relevant topic [7, 19]. Moreover, new properties may arise with new synthesis routes [8, 10]. Besides that, the often used birnessite synthesis routes present some drawbacks, particularly related to long-time duration. Hydrothermal routes may be relatively fast, lasting about 30 min, but require elaborated high temperature and pressure apparatuses [20–23]. Sol–gel processes may require even higher temperatures, several hours of reaction and steps [24]. Even newer methods, that avoid the use of high-temperature or pressure treatment, still have duration as disadvantage. For instance, a polyol-reflux method requires a 1 h reaction [25] and another demands a statically aging of 1 day [15]. Electrochemical deposition [18, 26], in its turn, is limited to the production of low dimensions films [27].

Therefore, in this work we suggest a novel and simple chemical route for selective δ-MnO_2 synthesis with high specific capacitance. Our method is based on the reduction of potassium permanganate ($KMnO_4$) [28] with nascent hydrogen. Nascent hydrogen (H^*) reduction is a well spread method for the obtainment of several compounds [29, 30]. The metastable hydrogen form, produced on the reduction of metals in acid medium, tends to combine quickly to form H_2, but during its short lifetime it is a highly reactive reduction agent [30, 31]. The production of δ-MnO_2 by such method has the advantages of being a very quick, one-pot reaction, sprinted at low temperature. Reaction duration is lower than ten minutes. In addition,

the final product may be used as suspension (as synthesized) or as powder (after drying) and procedure required only simple laboratory glassware. Such innovative method was firstly developed by our group for the obtainment of transition metal oxide and graphene nanocomposites, showing singular results [32]. To the best of our knowledge, this is the first time that reduction by H^* is employed to the fabrication of any kind of manganese oxide.

2 Materials and methods

Firstly, 100 mL of an aqueous solution of 10 mmol L^{-1} $KMnO_4$ ($\geq$ 99.0%, Sigma-Aldrich) was prepared and transferred to a round-bottomed flask. The same volume of a previously cooled 2 mol L^{-1} hydrochloric acid (Synth) solution was added to the flask. The resulting solution was kept in ice bath until temperature stabilization in approximately 10 °C. Then, 1.65 g of magnesium metallic foils (Vetec) was added to the solution, starting the reaction. By the end of the exothermic reaction, that lasted about 10 min, a dark brown precipitate was formed. The product was washed with deionized water by centrifugation. After that, the precipitate was dried at 100 °C by 24 h. The whole procedure is illustrated in Fig. 1.

X-ray diffractogram was acquired in a diffractometer (Shimadzu XRD-6000) with CuKα radiation (λ = 1.5418 Å), 40 kV voltage and 40 mA current. For all other characterization techniques, the powder was dispersed in ethanol, drop casted in silicon (Si/SiO$_2$) wafers and dried for 24 h at 65 °C. Raman spectrum was collected in a Raman spectrometer (Witec UHTS 300 VIS) with 488 nm nominal wavelength laser excitation line. Attenuated Total Reflectance Fourier Transformed Infrared (ATR-FTIR) spectrum was collected in a spectrophotometer (Shimadzu IRAffinity-1S
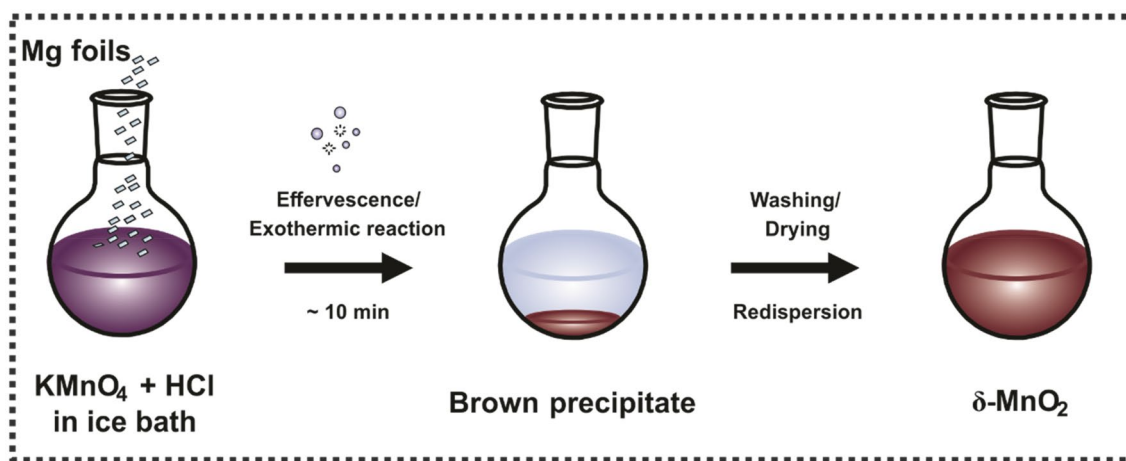

Fig. 1 Schematic representation of the δ-MnO_2 synthesis procedure

FTIR) with 4 cm^{-1} resolution and 32 accumulations. X-ray photoelectron spectroscopy (XPS) analysis was performed on a photoelectron spectrometer (Thermo Scientific™ XPS K-Alpha™) using a 72 W Al Kα X-ray source and a monochromator with 400 μm spot size with 5 μm step. Curve fitting and background subtraction were accomplished using Avantage 5.977 (Thermo Scientific™) software. Scanning electron microscopy (SEM) images were obtained in a scanning electron microscope (TESCAN MIRA3) operated at 10 kV with an In-Beam detector.

Electrochemical measurements were performed in a potentiostat/galvanostat (Metrohm Autolab PGSTAT302N) in three electrodes cell. For working electrodes preparation, the obtained δ-MnO$_2$ powder was dispersed in deionized water, drop casted in a 1 cm^2 area of fluorine doped tin oxide (FTO) substrate and dried for 24 h at 65 °C. The electrolyte was an aqueous solution of 0.5 mol L^{-1} sodium sulfate (Na$_2$SO$_4$). Reference and counter electrodes were silver/silver chloride (Ag/AgCl) and platinum wire, respectively.

3 Results and discussion

Nascent hydrogen could be produced from the oxidation of metals as magnesium, aluminum, iron or zinc [30]. For convenience we choose Mg, which standard reduction potential is $E^0(Mg^{2+}/Mg) = -2.372V$ [33], compatible with the H$^+$/H* couple estimated $E^0(H^+/H^*) = -2.106V$ [31]. Thus, the formation of the nascent hydrogen is spontaneous upon Mg oxidation in acid media [31], following the Eq. 1.

$$Mg + 2H^+ \rightarrow Mg^{2+} + 2H^* \tag{1}$$

This was confirmed through vigorous effervescence of hydrogen bubbles and a small increase in the temperature was also observed when the metal was added to the solution. The reaction was considered ended few minutes later, when the effervescence was finished, and all the Mg was consumed. By that moment, it was noticeable that the previous vivid-purple KMnO$_4$ solution changed to a transparent solution with a large amount of a brownish precipitate, as described in Fig. 1.

In order to confirm the formation of the desired birnessite and to acquire detailed information about the product, we performed structural and morphological characterizations.

Figure 2a shows the diffractogram for the MnO$_2$ powder. The diffractogram shows four distinct peaks centered in 12.08°, 23.11°, 37.96° and 66.22°. Several authors [2, 10, 11, 22, 34] attributed similar patterns to K-birnessite-type manganese dioxide, following JCPDS 80–1098 card. According to the card, those peaks may be ascribed to

Fig. 2 **a** X-Ray diffractogram of δ-MnO$_2$ (red line) and pattern of related JCPDS card No. 80–1098 (blue line); **b** Raman spectrum of δ-MnO$_2$, and **c** ATR-FTIR spectrum of δ-MnO$_2$
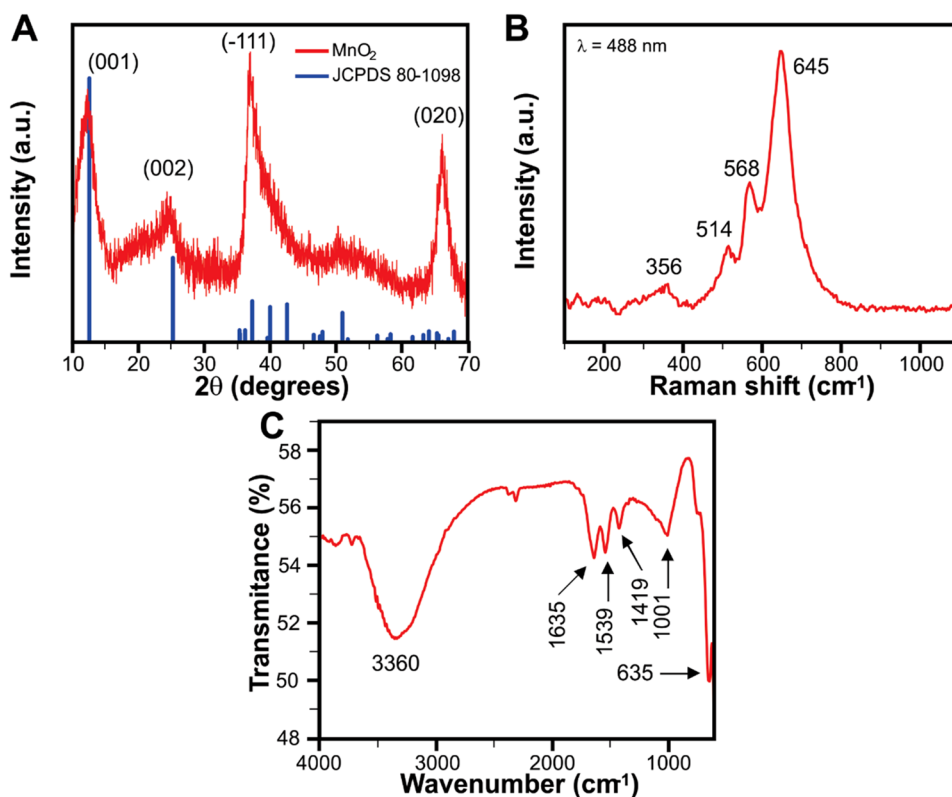
(001), (002), (−111) and (020) planes, respectively. We highlight that powdered specimens contain very small crystallites arranged in completely random orientations. Because of that, powder lines have a significant width and tend to merge or overlap [35], becoming broad peaks. That may have happened with the several lines that occur in the (−111) and (020) peaks region, resulting in the intense and broad 37.96° and 66.22° peaks in our diffractogram. Besides that, the diffractogram presents a significant high signal–noise ratio. That is also a consequence of powder diffraction, where many reflections with low resolution are available [35]. Regarding to the structure, according to previous studies, the alkaline cation K+ in the medium acts as a nanosheet stabilizer, thus favoring the formation of the layered structure [22]. The position of the (001) peak reveals an interlayer distance of 7.32 Å, in accordance with other birnessites reported in the literature [2, 10, 13, 22].

Although birnessite has low Raman activity and accuracy, the technique was helpful to further understanding the oxide structure. The Raman spectrum of the δ-MnO_2 is presented in Fig. 2b. Three of the expected bands aroused in 645, 568 and 514 cm^{-1}. The 645 cm^{-1} band was assigned to the A_{1g} symmetric mode, ascribed to the symmetric stretching vibration v_2(Mn–O) of [MnO_6] groups. The 568 cm^{-1} band was assigned to the v_3(Mn–O) symmetric stretching vibration in the basal plane of [MnO_6] sheets [13]. On the other hand, the red shift of the 514 cm^{-1} band (v_4), comparing to other reports, and the appearance of

a fourth mode (v_7) at around 356 cm^{-1} may be related to v(K–O) vibrations [13, 23].

Combined with others, FTIR is a powerful technique to evaluate materials structure. The ATR-FTIR spectrum, illustrated in Fig. 2c, exhibits six assignable bands: 635, 1001, 1419, 1539, 1635 and 3360 cm^{-1}. All these modes were compatible with birnessite samples [36, 37]. The band at 635 cm^{-1} was attributed to v(Mn–O) lattice vibrations of poorly ordered birnessites. The band at 1001 cm^{-1} was related to v(Mn(III)–OH) in the layer basal plane, thus evidencing the presence of Mn(III) simultaneously with the predominant Mn(IV). The bands within the 4000–1400 cm^{-1} range were assigned to.

−OH stretching (v) and bending (δ) vibrational modes [36]. The one in 1419 cm^{-1} is related to hydroxide groups located at specific crystallographic sites, while the others are related to less ordered water groups [37]. The presence and position of those four Raman and these six FTIR modes ratified the DRX findings about the δ-MnO_2.

The surface chemical composition of the δ-MnO_2 was further analyzed by XPS to clarify the oxidation states of the oxide components. As shown in Fig. 3a, Mn2p, O1s and Mg1s peaks were present on the survey. From that, composition of the sample surface was determined as 31.7% of Mn, 66.1% of O and 2.2% of Mg. Magnesium in the structure, evidenced by the peak at 1303.15 eV, derived from the metal/acid reaction. From Fig. 3b, the position of the Mn2p main peaks – $Mn2p_{1/2}$ at 654.1 eV and $Mn2p_{3/2}$

Fig. 3 **a** Survey XPS spectrum of the δ-MnO_2; **b** Mn2p; **c** deconvoluted $Mn2p_{3/2}$ and **d** deconvoluted O1s XPS spectra of the δ-MnO_2
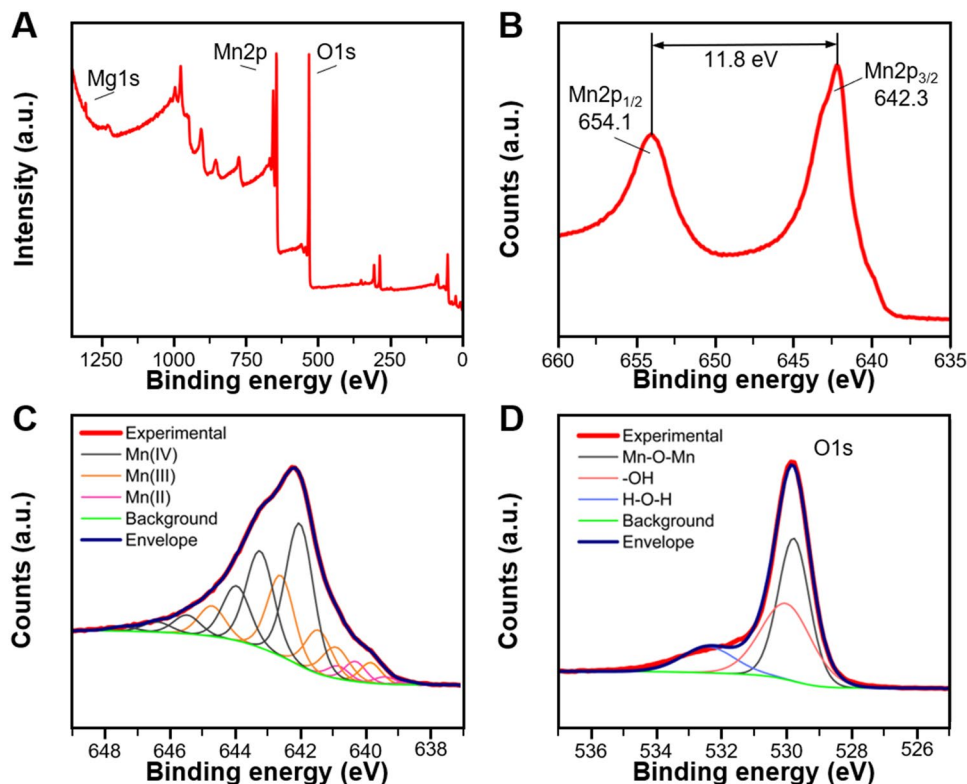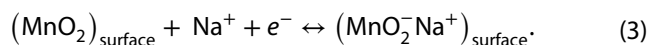
at 642.3 eV and the spin-energy separation of 11.8 eV between them are in accordance with the main MnO_2 XPS studies [38–41]. Similarly, works dedicated to the synthesis of MnO_2 [42–45] found similar values. $Mn2p_{3/2}$ was further analyzed for the determination of the different Mn oxidation states composition. According to Nesbitt and Banerjee [38], the $Mn2p_{3/2}$ peak of birnessites can be deconvoluted in five multiplets for each manganese valence. Following these authors, we deconvoluted the $Mn2p_{3/2}$ peak fixing the FWHM of the multiplets as done by Sun and coworkers [46], as shown in Fig. 3c. The resulting Mn valences composition was calculated as 58.3% Mn(IV), 35.0% Mn(III) and 6.7% Mn(II). Comparing with Sun and coworkers [46], we observed a higher Mn(III) content to the detriment of Mn(IV). However, this composition is similar to some of the verified by Ilton and coworkers when obtained from the $Mn2p_{3/2}$ peak deconvolution [40]. Moreover, Athouël and coworkers [16] proved that higher Mg(III)/Mg(IV) ratio is usual when the synthesis of birnessite occurs in the presence of Mg. Following the same methodology, we proceeded the analysis of the O1s peak. As shown in Fig. 3d, the O1s peak showed a maximum at 529.9 eV and a broad shoulder at higher energies, being this another evidence that the synthesized oxide is a birnessite [38]. The main contribution of O1s peak is given by the oxide structural oxygen (Mn–O–Mn), representing 46.4% of the spectrum. The two other peaks with maximums in 530.1 and 532.4 eV were attributed to the presence of structurally bounded hydroxide (–OH) (39.6%) and adsorbed water (H–O–H) (14.0%), respectively. The structural oxygen is lower than the reported by other authors [46, 47]. However, it is a consequence of the lower Mn(IV) availability. Besides all the

XPS being compatible with birnessite-type MnO_2, these results agreed with the previously attested on FTIR.

The morphology of the δ-MnO_2 synthesized through H^* reduction of $KMnO_4$ was investigated by SEM. The lower magnification image, shown in Fig. 4a, revealed aggregates of randomly shaped structures with some microns of dimension. Higher magnification image, shown in Fig. 4b, indicated that the oxide structure is porous and built up of many nanosheets, similar to nanoflower structures. These features are typical of δ-MnO_2 obtained by hydrothermal routes [20, 21, 23].

As the structural and morphological characterization are in accordance with the δ-MnO_2 features, we evaluated the electrochemical performance of this structure as electrode for electrochemical capacitors.

According to the literature, sodium sulfate is one of the most suitable electrolyte for manganese oxides [48]. Na^+ cations are appropriate to be intercalated in the bulk of MnO_2 upon reduction and deintercalated upon oxidation [48, 49] following the Eq. 2 or to be adsorbed on the surface of the oxide by following the Eq. 3.

$$MnO_2 + Na^+ + e^- \leftrightarrow MnOONa \qquad (2)$$

$$\left(MnO_2\right)_{surface} + Na^+ + e^- \leftrightarrow \left(MnO_2^- Na^+\right)_{surface}. \qquad (3)$$

In general, MnO_2 electrodes present pseudocapacitive behavior, showing nearly rectangular-shaped voltammograms [10, 18, 20, 25]. In birnessite arrangement, however, the electron transfer that takes place in the Mn(IV)/Mn(III) redox system, described by the Eq. 2, is usually visible through cathodic and anodic peaks [10, 15, 50]. Depending
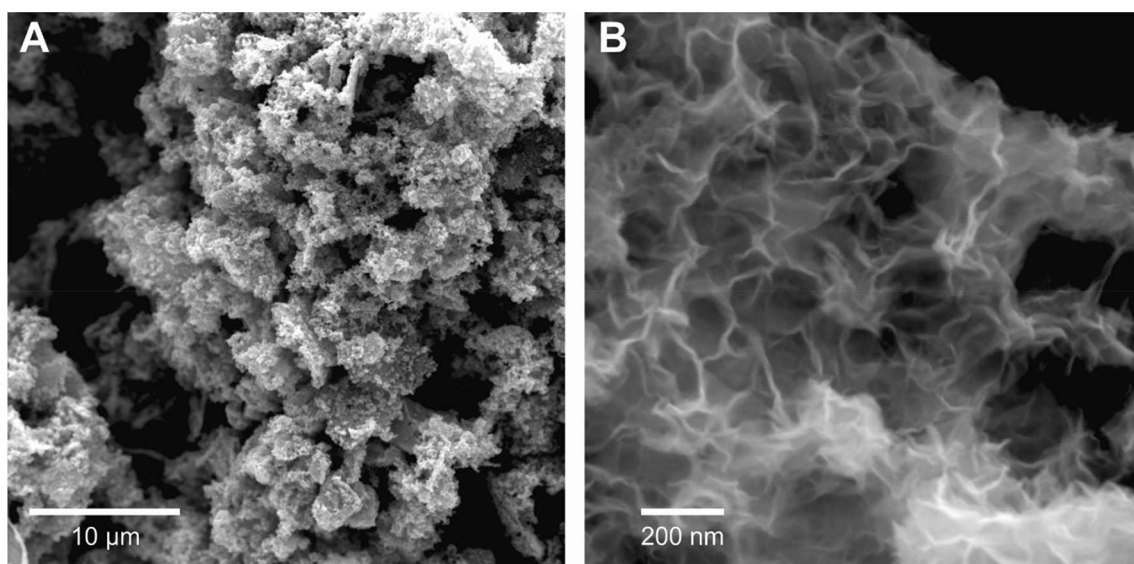

Fig. 4 SEM images of δ-MnO_2 with **a** lower and **b** higher magnification

on the involved constituents, sometimes even more than one peak of each type may arise [16, 49, 51, 52]. Figure 5a shows the cyclic voltammogram of the δ-MnO$_2$ between − 0.1 and 0.9 V in different scan rates (5–100 mV s^{-1}). Both expected electrochemical processes were perceptible. The anodic peak occurred between 0.55 and 0.71 V, and the cathodic peak between 0.35 and 0.51 V, depending on the scan rate. This redox process may reflect the redox transitions of the manganese, including Mn^{3+}/Mn^{2+}, Mn^{4+}/Mn^{3+} and Mn^{6+}/Mn^{4+} or can be related to the cation deintercalation upon oxidation and cation insertion upon reduction [10]. These values are highly comparable with the ones of the cited reports [10, 15, 50].

Figure 5b shows the plot of peak currents (I$_p$) versus potential scan rate. The linearity of the plots confirms the redox behavior of the storage reaction [53]. However, for an exclusively redox reaction the ratio of the modulus of the anodic and cathodic peak currents (I$_{p,a}$/I$_{p,c}$) in all scan rates should equal to 1 [53, 54]. Noticeably the modulus of the curves slopes differs from each other, thus implying in a varying I$_{p,a}$/I$_{p,c}$. Differences between anodic and cathodic peaks is a recurrent feature of birnessites [49, 51]. Kanoh and coworkers [51] suggested that it could be an implication of differences of mechanisms of kinetics between intercalation and deintercalation processes, what was later experimentally confirmed by Athouël and colleagues [49].

Specific capacitance is usually valued through galvanostatic charge/discharge measurement. Performed galvanostatic charge/discharge curves at different current densities (0.25–2.00 A g^{-1}) are plotted in Fig. 5c. The shape of the charge and discharge curves of potential as function of time are typical of faradaic electrochemical capacitors

Fig. 5 δ-MnO$_2$ **a** cyclic voltammograms at 5, 10, 20, 50 and 100 V s^{-1} scan rate; **b** cyclic voltammetry anodic and cathodic peak currents (I$_p$) as function of the scan rate; **c** charge and discharge curves at 0.25, 0.50, 1.00 and 2.00 A g^{-1}; **d** specific capacitances and standard deviation in each current density and **e** capacitance retention through 500 cycles. All performed in 0.5 mol L^{-1} Na$_2$SO$_4$ electrolyte
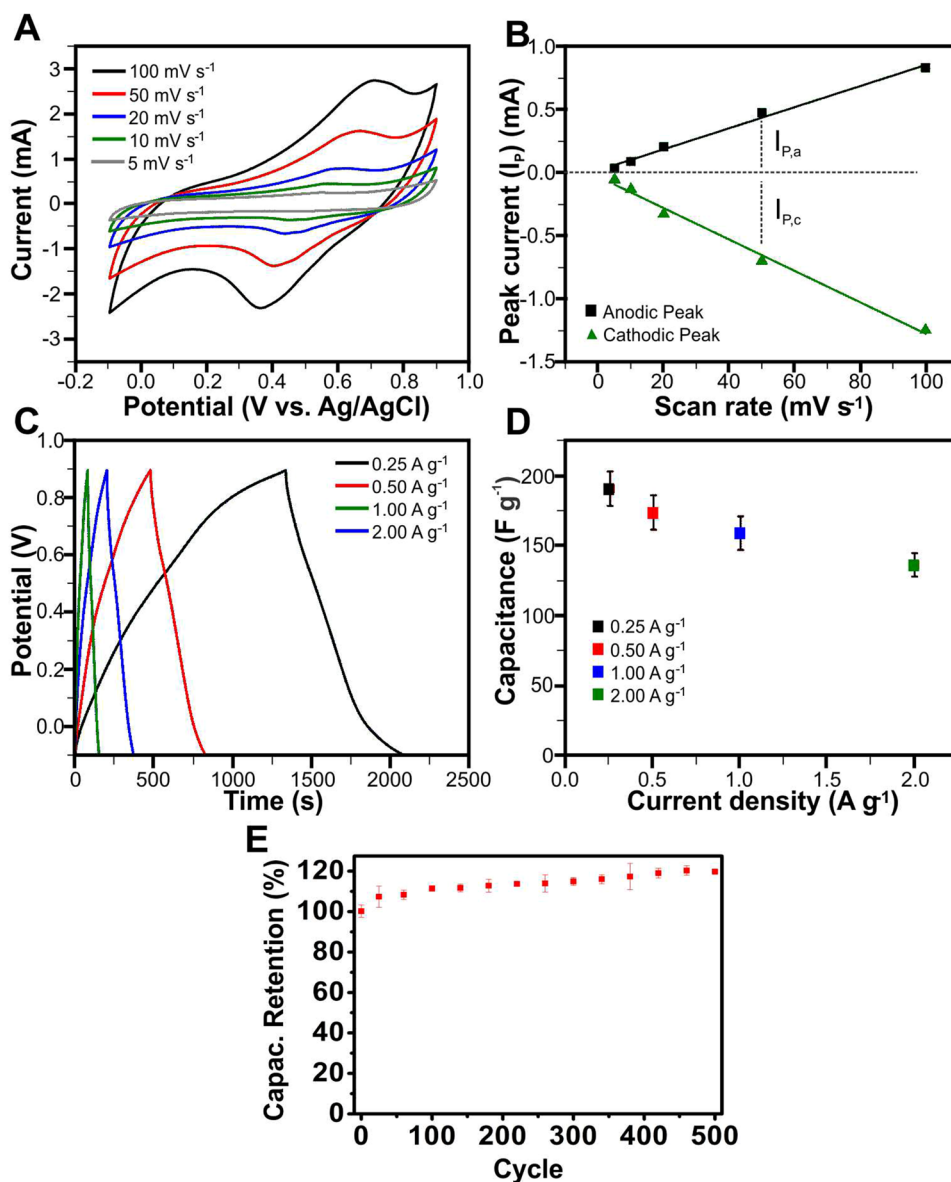
[14]. Specific capacitances (C_s) were calculated using the Eq. 4, where i is the discharge current, Δt is the discharge time, m is the mass of the active material in the electrode, and ΔV is the potential window of cycling.

$$C_s = (i\Delta t)/(m\Delta V). \tag{4}$$

The results were plotted in Fig. 5d, where one can see that the best specific capacitance of 190 ± 12 F g^{-1} was obtained at 0.25 A g^{-1} current density. When the current density was increased to 0.50, 1.00 and 2.00 A g^{-1}, measured specific capacitances were 173 ± 12, 158 ± 12 and 136 ± 8 F g^{-1}, respectively. These high capacitance values are typical of δ-MnO$_2$ thin film electrodes reported [16, 18, 50] with the additional advantages of being produced very quickly, without requiring external energy provision, long furnace dwell times nor sophisticated laboratory apparatuses.

It is worth mentioning that all the electrochemical reported data was recorded after an electrode stabilization. As evidenced on the long-term cycling stability shown in Fig. 5e, the electrode rapidly gains capacitance in the first cycles and remains relatively stable after this. Such phenomenon is well discussed in the literature, once many authors report the capacitances and capacitance retention only after stabilization [10]. Thus, the capacitance gain may be related to several ongoing processes, as wettability improvement and self-activation [55, 56] over the cycles. Beyond wettability improvement, the electroactivation in our birnessite may be related to the presence of Mg (evidenced by XPS). Athouël and colleagues [16] showed that magnesium is exchanged by sodium ions (Na$^+$) by simply soaking the electrode in the electrolyte solution. Upon the exit of the retained Mg, especially in the initial cycles, more electroactive sites are released, increasing the capacitance.

4 Conclusions

We successfully synthesized a high capacitive birnessite-type MnO$_2$ by a novel simple route based on the reduction of KMnO$_4$ by nascent hydrogen. The volatile metastable hydrogen form was generated by the reduction of magnesium foil in acid media. DRX characterization showed that the as-synthesized MnO$_2$ has a layered structure, with interlayer space of 7.13 Å and nanoscale sized crystallite. Raman and FTIR techniques confirmed DRX findings and evidenced the presence of Mn(III) and Mn(II) apart to the predominant Mn(IV). By XPS, it was confirmed the presence of Mn in different valence states and a residual Mg. Morphology was clarified by SEM, that showed randomly shaped porous structures formed by nanosheets aggregates.

Finally, we evaluated the electrochemical activity of the as-synthesized δ-MnO$_2$ in Na$_2$SO$_4$. The oxide showed a redox behavior and specific capacitance as high as 190 F g^{-1} at 0.25 A g^{-1} current density. Thus, the developed synthesis route for high capacitive δ-MnO$_2$ was found to be advantageous by being fast, selective, driven at low temperature with only simple laboratory glassware.

Compliance with ethical standards

Conflicts of interest The authors declare that they have no conflicts of interest.

References

1. Simon P, Gogotsi Y (2008) Materials for electrochemical capacitors. Nat Mater 7:845–854. https://doi.org/10.1142/9789814287005_0033
2. Li F, Xing Y, Huang M et al (2015) MnO2 nanostructures with three-dimensional (3D) morphology replicated from diatoms for high-performance supercapacitors. J Mater Chem A 3:7855–7861. https://doi.org/10.1039/c5ta00634a
3. Pistoia G (1982) Some restatements on the nature and behavior of MnO2 for Li batteries. J Electrochem Soc 129:1861–1865. https://doi.org/10.1149/1.2124315
4. Moses PR, Taylor AH, Turchan MJ (1983) Non-Aqueous Li/MnO2 Cell. US Patent number 4,401,735.
5. David WIF, Thackeray MM, Goodenough JB (1984) Lithium insertion into β-MnO2 and the rutile-spinel transformation. Mater Res Bull 19:99–106. https://doi.org/10.1016/0025-5408(84)90015-1
6. Lee HY, Manivannan V, Goodenough JB (1999) Electrochemical capacitors with KCl electrolyte. Comptes Rendus l'Academie des Sci - Ser IIc Chem 2:565–577. https://doi.org/10.1016/S1387-1609(00)88567-9
7. Wei W, Cui X, Chen W, Ivey DG (2011) Manganese oxide-based materials as electrochemical supercapacitor electrodes. Chem Soc Rev 40:1697–1721. https://doi.org/10.1039/c0cs00127a
8. Brock SL, Duan N, Tian ZR et al (1998) A review of porous manganese oxide materials. Chem Mater 10:2619–2628. https://doi.org/10.1021/cm980227h
9. Kitchaev DA, Peng H, Liu Y et al (2016) Energetics of MnO2 polymorphs in density functional theory. Phys Rev B 93:1–5. https://doi.org/10.1103/PhysRevB.93.045132
10. Ghodbane O, Pascal JL, Favier F (2009) Microstructural effects on charge-storage properties in MnO2-based electrochemical supercapacitors. ACS Appl Mater Interfaces 1:1130–1139. https://doi.org/10.1021/am900094e
11. Sun Y, Xu C, Li B, et al (2014) Synthesis of single-crystalline limn2o4 with different dimensional nanostructures for li-ion batteries. Int J Electrochem Sci 9:6387–6401. https://doi.org/N/A

12. Anthony JW, Bideaux RA, Bladh KW, Nichols MC handbook of mineralogy. mineralogical society of america, chantilly, VA 20151–1110, USA. https://www.handbookofmineralogy.org/.

13. Julien C, Massot M, Baddour-Hadjean R et al (2003) Raman spectra of birnessite manganese dioxides. Solid State Ionics 159:345–356. https://doi.org/10.1016/S0167-2738(03)00035-3

14. Brousse T, Bélanger D, Long JW (2015) To be or not to be pseudocapacitive? J Electrochem Soc 162:A5185–A5189. https://doi.org/10.1149/2.0201505jes

15. Ghodbane O, Ataherian F, Wu NL, Favier F (2012) In situ crystallographic investigations of charge storage mechanisms in MnO2-based electrochemical capacitors. J Power Sources 206:454–462. https://doi.org/10.1016/j.jpowsour.2012.01.103

16. Athouël L, Moser F, Dugas R et al (2008) Variation of the MnO2 birnessite structure upon charge/discharge in an electrochemical supercapacitor electrode in aqueous Na2SO4 electrolyte. J Phys Chem C 112:7270–7277. https://doi.org/10.1021/jp0773029

17. Subramanian V, Zhu H, Vajtai R et al (2005) Hydrothermal synthesis and pseudocapacitance properties of MnO2 nanostructures. J Phys Chem B 109:20207–20214. https://doi.org/10.1021/jp0543330

18. Zhou YK, Toupin M, Bélanger D et al (2006) Electrochemical preparation and characterization of Birnessite-type layered manganese oxide films. J Phys Chem Solids 67:1351–1354. https://doi.org/10.1016/j.jpcs.2006.01.069

19. Cheng Q, Tang J, Ma J et al (2011) Graphene and nanostructured MnO2 composite electrodes for supercapacitors. Carbon N Y 49:2917–2925. https://doi.org/10.1016/j.carbon.2011.02.068

20. Zhang X, Yu P, Zhang H et al (2013) Rapid hydrothermal synthesis of hierarchical nanostructures assembled from ultrathin birnessite-type MnO2 nanosheets for supercapacitor applications. Electrochim Acta 89:523–529. https://doi.org/10.1016/j.electacta.2012.11.089

21. Li Y, Wang J, Zhang Y et al (2012) Facile controlled synthesis and growth mechanisms of flower-like and tubular MnO2 nanostructures by microwave-assisted hydrothermal method. J Colloid Interface Sci 369:123–128. https://doi.org/10.1016/j.jcis.2011.12.013

22. Aziz RA, Jose R (2017) Charge storage capability of tunnel MnO2 and alkaline layered Na-MnO2 as anode material for aqueous asymmetry supercapacitor. J Electroanal Chem 799:538–546. https://doi.org/10.1016/j.jelechem.2017.06.014

23. Sinha AK, Pradhan M, Pal T (2013) Morphological evolution of two-dimensional MnO2 nanosheets and their shape transformation to one-dimensional ultralong MnO2 nanowires for robust catalytic activity. J Phys Chem C 117:23976–23986. https://doi.org/10.1021/jp403527p

24. Franger S, Bach S, Farcy J et al (2002) Synthesis, structural and electrochemical characterizations of the sol-gel birnessite MnO1.84·0.6H2O. J Power Sources 109:262–275. https://doi.org/10.1016/S0378-7753(02)00072-1

25. Zhou J, Yu L, Sun M et al (2013) Novel synthesis of birnessite-type MnO2 nanostructure for water treatment and electrochemical capacitor. Ind Eng Chem Res 52:9586–9593. https://doi.org/10.1021/ie400577a

26. Pinaud BA, Chen Z, Abram DN, Jaramillo TF (2011) Thin films of sodium birnessite-type MnO2: optical properties, electronic band structure, and solar photoelectrochemistry. J Phys Chem C 115:11830–11838. https://doi.org/10.1021/jp200015p

27. Laforgue A, Simon P, Sarrazin C, Fauvarque JF (1999) Polythiophene-based supercapacitors. J Power Sources 80:142–148. https://doi.org/10.1016/S0378-7753(98)00258-4

28. Liu X, Chen C, Zhao Y, Jia B (2013) A review on the synthesis of manganese oxide nanomaterials and their applications on lithium-ion batteries. J Nanomater 2013:1–7. https://doi.org/10.1155/2013/736375

29. Domingues SH, Kholmanov IN, Kim T et al (2013) Reduction of graphene oxide films on Al foil for hybrid transparent conductive film applications. Carbon N Y 63:454–459. https://doi.org/10.1016/j.carbon.2013.07.007

30. Pham VH, Pham HD, Dang TT et al (2012) Chemical reduction of an aqueous suspension of graphene oxide by nascent hydrogen. J Mater Chem 22:10530–10536. https://doi.org/10.1039/c2jm30562c

31. Laborda F, Bolea E, Baranguan MT, Castillo JR (2002) Hydride generation in analytical chemistry and nascent hydrogen: When is it going to be over? Spectrochim Acta Part B 57:797–802. https://doi.org/10.1016/S0584-8547(02)00010-1

32. Pieretti JC, Trevisan TB, de Moraes MMM et al (2019) High capacitive rGO/WO3 nanocomposite: the simplest and fastest route of preparing it. Appl Nanosci. https://doi.org/10.1007/s13204-019-01089-z

33. Lide DR (2006) CRC Handbook of Chemistry and Physics. CRC Press/Taylor and Francis Group, Boca Raton, FL

34. Wang M, Zhang L, Huang W et al (2017) Pt/MnO2 nanosheets: facile synthesis and highly efficient catalyst for ethylene oxidation at low temperature. RSC Adv 7:14809–14815. https://doi.org/10.1039/c6ra26529d

35. Ladd M, Palmer R (2013) structure determination by x-ray crystallography. Fifth, Springer, New York

36. Zhao W, Liu F, Feng X et al (2012) Fourier transform infrared spectroscopy study of acid birnessites before and after Pb2+ adsorption. Clay Miner 47:191–204. https://doi.org/10.1180/claymin.2012.047.2.04

37. Potter RM, Rossman GR (1979) The tetravalent manganese oxides: identification, hydration, and structural relationships by infrared spectroscopy. Am Mineral 64:1199–1218

38. Nesbitt HW, Banerjee D (1998) Interpretation of XPS Mn(2p) spectra of Mn oxyhydroxides and constraints on the mechanism of MnO2 precipitation. Am Mineral 83:305–315. https://doi.org/10.2138/am-1998-3-414

39. Audi AA, Sherwood PMA (2002) Valence-band X-ray photoelectron spectroscopic studies of manganese and its oxides interpreted by cluster and band structure calculations. Surf Interface Anal 33:274–282. https://doi.org/10.1002/sia.1211

40. Ilton ES, Post JE, Heaney PJ et al (2016) XPS determination of Mn oxidation states in Mn (hydr)oxides. Appl Surf Sci 366:475–485. https://doi.org/10.1016/j.apsusc.2015.12.159

41. Biesinger MC, Payne BP, Grosvenor AP et al (2011) Resolving surface chemical states in XPS analysis of first row transition metals, oxides and hydroxides: Cr, Mn, Fe, Co and Ni. Appl Surf Sci 257:2717–2730. https://doi.org/10.1016/j.apsusc.2010.10.051

42. Yan J, Fan Z, Wei T et al (2010) Fast and reversible surface redox reaction of graphene-MnO2 composites as supercapacitor electrodes. Carbon N Y 48:3825–3833. https://doi.org/10.1016/j.carbon.2010.06.047

43. Ren Z, Li J, Ren Y et al (2016) Large-scale synthesis of hybrid metal oxides through metal redox mechanism for high-performance pseudocapacitors. Sci Rep 6:1–10. https://doi.org/10.1038/srep20021

44. Pang M, Long G, Jiang S et al (2015) One pot low-temperature growth of hierarchical δ-MnO2 nanosheets on nickel foam for supercapacitor applications. Electrochim Acta 161:297–304. https://doi.org/10.1016/j.electacta.2015.02.089

45. Kalubarme RS, Jadhav HS, Park CJ (2013) Electrochemical characteristics of two-dimensional nano-structured MnO2 for symmetric supercapacitor. Electrochim Acta 87:457–465. https://doi.org/10.1016/j.electacta.2012.09.081

46. Sun X, Duffort V, Mehdi BL et al (2016) Investigation of the mechanism of Mg insertion in birnessite in nonaqueous and aqueous

rechargeable Mg-ion batteries. Chem Mater 28:534–542. https://doi.org/10.1021/acs.chemmater.5b03983

47. Yan D, Yan P, Cheng S et al (2009) Fabrication, in-depth characterization, and formation mechanism of crystalline porous birnessite MnO2 film with amorphous bottom layers by hydrothermal method. Cryst Growth Des 9:218–222. https://doi.org/10.1021/cg800312u

48. Toupin M, Brousse T, Bélanger D (2004) Charge storage mechanism of mno2 electrode used in aqueous electrochemical capacitor. Chem Mater 16:3184–3190. https://doi.org/10.1021/cm049649j

49. Athouël L, Moser F, Dugas R et al (2008) Birnessite as possible candidate for hybrid Carbon/MnO2 electrochemical capacitor. ECS Trans 16:119–123. https://doi.org/10.1149/1.2985634

50. Brousse T, Toupin M, Dugas R et al (2006) Crystalline MnO2 as possible alternatives to amorphous compounds in electrochemical supercapacitors. J Electrochem Soc 153:A2171. https://doi.org/10.1149/1.2352197

51. Kanoh H, Tang W, Makita Y, Ooi K (1997) Electrochemical intercalation of alkali-metal ions into birnessite-type manganese oxide in aqueous solution. Langmuir 13:6845–6849. https://doi.org/10.1021/la970767d

52. Alfaruqi MH, Gim J, Kim S et al (2015) A layered δ-MnO2 nanoflake cathode with high zinc-storage capacities for eco-friendly battery applications. Electrochem commun 60:121–125. https://doi.org/10.1016/j.elecom.2015.08.019

53. de Silva C, CC e, Breitkreitz MC, Santhiago M, et al (2012) Construction of a new functional platform by grafting poly(4-vinylpyridine) in multi-walled carbon nanotubes for complexing copper ions aiming the amperometric detection of L-cysteine. Electrochim Acta 71:150–158. https://doi.org/10.1016/j.electacta.2012.03.114

54. Bard AJ, Faulkner LR (2001) Electrochemical methods: fundamentals and applications. Wileys, New York

55. Xu K, Li S, Yang J et al (2016) Hierarchical MnO2 nanosheets on electrospun NiCo2O4 nanotubes as electrode materials for high rate capability and excellent cycling stability supercapacitors. J Alloys Compd 678:120–125. https://doi.org/10.1016/j.jallcom.2016.03.255

56. Ling Z, Wang Z, Zhang M et al (2016) Sustainable Synthesis and Assembly of Biomass-Derived B/N Co-Doped Carbon Nanosheets with Ultrahigh Aspect Ratio for High-Performance Supercapacitors. Adv Funct Mater 26:111–119. https://doi.org/10.1002/adfm.201504004